INTERNATIONAL JOURNAL FOR NUMERICAL METHODS IN FLUIDS
Int. J. Numer. Meth. Fluids 2017; **00**:1–21
Published online in Wiley Online Library (www.onlinelibrary.wiley.com). DOI: 10.1002/fld.4480

Novel local smoothness indicators for improving the third-order WENO scheme

Shengping Liu[1,2],Yiqing Shen[1,2*], Bei Chen[1,2], Fangjun Zeng[1,2]

[1] *State Key Laboratory of High Temperature Gas Dynamics, Institute of Mechanics, Chinese Academy of Science, Beijing, China, 100190,*
[2] *School of Engineering Science, University of Chinese Academy of Sciences, Beijing, China, 100049*

SUMMARY

The local smoothness indicators play an important role in the performance of a weighted essentially non-oscillatory (WENO) scheme. Due to having only two points available on each sub-stencil, the local smoothness indicators calculated by conventional methods of Jiang and Shu[1] make the third-order WENO scheme too dissipative. In this paper, we propose a different method to calculate the indicators by using all the three points on the global stencil of the third-order WENO scheme. The numerical results demonstrate that the WENO scheme with the new indicators has less dissipation and better resolution than the ones of Jiang and Shu's for both smooth and discontinuous solutions. Copyright © 2017 John Wiley & Sons, Ltd.

Received . . .

KEY WORDS: third-order WENO scheme; local smoothness indicator; numerical dissipation

1. INTRODUCTION

The weighted essentially non-oscillatory (WENO) scheme was first proposed by Liu et al.[2]. The main idea is that, instead of choosing the smoothest stencil in the ENO (essentially non-oscillatory) scheme[3], the WENO scheme uses a convex combination of all candidate stencils (sub-stencils) to obtain high order accuracy in smooth regions while keeping the ENO property near shock waves. The analysis of Jiang and Shu[1] showed that, with the local smoothness indicators introduced by Liu et al.[2], the WENO scheme constructed from the rth order ENO scheme is only $(r+1)$th order accurate. Then, Jiang and Shu[1] proposed a classical way to calculate the local smoothness indicators, with which the WENO (WENO-JS) scheme can achieve $(2r-1)$th

*Correspondence to: State Key Laboratory of High Temperature Gas Dynamics, Institute of Mechanics, Chinese Academy of Science, No.15 Beisihuanxi Road, Beijing, China, 100190, E-mail: yqshen@imech.ac.cn

order. Balsara and Shu[4] extended the WENO schemes up to eleventh-order and designed a class of monotonicity preserving WENO schemes. However, Henrick et al.[5] pointed out that the indicators of Jiang and Shu[1] failed to improve the accuracy of WENO scheme at critical points and then proposed a mapping function to modify the weights. The new WENO (WENO-M) scheme can achieve the optimal convergence order at critical points. Gerolymos et al.[6] further extended both WENO-JS and WENO-M schemes up to the seventeenth-order. In [7], Borges et al. designed a global smoothness indicator (WENO-Z scheme) to improve the accuracy of the fifth-order WENO-JS scheme directly. Later, Castro et al.[8] developed higher order WENO-Z schemes. Ha et al.[9] derived a different method that measures the local smoothness of the numerical solution inside a stencil and devised a sixth-order global smoothness indicator to construct the fifth-order WENO-Z-type scheme. Recently, Fan et al.[10] constructed higher order (up to eighth-order) global smoothness indicators, with which the associated WENO-Z-type schemes can obtain fifth convergence order in smooth regions, even at the second order critical points where both the first and second derivatives vanish.

Compared with higher order WENO schemes, the third-order one has several advantages, for example, it is more robust for shock problems, it uses less grid points and hence it reduces the difficulty of boundary treatment and can be easily generalized to unstructured meshes, and also it provides a suitable compromise of the computation cost and the accuracy in some cases. However, the third-order WENO scheme with the smoothness indicators of Jiang and Shu[1] is too dissipative. And those techniques, such as the mapping function of WENO-M scheme[5] and the global stencil indicator of WENO-Z scheme[7], can effectively improve the accuracy of higher order WENO schemes[5, 6, 7, 8], but they cannot get satisfactory improvement on the third-order one. In [11], Yamaleev and Carpenter developed a third-order energy stable WENO (ESWENO) scheme, which can decrease the dissipation of the third-order WENO scheme apparently. However, the two tuning parameters ϵ and δ, which are designed for calculating the weight function and the artificial dissipation term of ESWENO scheme, are both dependent on the mesh size (or the total number of grid cells), and ϵ is also determined by the initial solution. Hence, the applications of the ESWENO scheme are limited. In [12], Wu et al. proposed a new global smoothness indicator and developed a less dissipative third-order WENO-Z-type (WENO-N3) scheme. Because WENO-N3 cannot reach the expected goal of high accuracy and low-dissipation, later, in [13], they suggested using the power function of the global indicator as the new one to construct the WENO-NP3 scheme. However, the new global smoothness indicator and the local smoothness indicators have different dimensions, this makes the results of the WENO-NP3 scheme uncertain in applications, in addition, WENO-NP3 generates apparent oscillatory solutions in many problems with shock waves.

As discussed in [1], the local smoothness indicators play a key role in the performance of a WENO scheme. Those works in [11, 12, 13] paid attention mainly to design the global smoothness indicators based on the two local smoothness indicators, which are calculated on each of sub-stencils. Hence, those improved third-order WENO schemes are still not so satisfactory. In this paper, we propose a novel way to calculate the two local smoothness indicators by using all three points on the global stencil. Analysis shows that, in monotonic smooth regions, the two new local indicators presented in this paper are the same, hence the calculated weights are equal to the optimal weights. Because of this important advantage, the new WENO scheme can greatly decrease the numerical dissipation.

This paper is organized as follows: in Section 2, we briefly describe the third-order WENO-JS scheme and some improved methods. The new local smoothness indicators and their properties are given in Section 3. In Section 4, various numerical examples are presented to validate the low dissipation property of the new scheme. Concluding remarks are given in Section 5.

2. THIRD-ORDER WENO SCHEMES

In this section, we briefly describe the WENO schemes by using the one-dimensional scalar conservative law equation[1]

$$\frac{\partial u}{\partial t}+\frac{\partial f}{\partial x}=0 \tag{1}$$

where $u(x,t)$ is a conserved quantity, $f(u)$ describes its flux, and x and t denote space and time, respectively. By defining the points $x_i = i\Delta x, (i = 0,\ldots,N)$, where Δx is the uniform grid spacing, the (1) can be approximated by a conservative finite difference formula

$$\frac{du_i}{dt}=-\frac{\hat{f}_{i+1/2}-\hat{f}_{i-1/2}}{\Delta x} \tag{2}$$

where $\hat{f}_{i\pm1/2}$ is the numerical flux.

The flux $\hat{f}_{i+1/2}$ of a third-order WENO scheme can be written as

$$\hat{f}_{i+1/2}=\omega_0 q_0+\omega_1 q_1 \tag{3}$$

where, q_k is the second-order flux on the sub-stencil $S_k = (i-1+k,\ i+k)$ and is given by

$$\begin{cases} q_0 = & -\frac{1}{2}f_{i-1}+\frac{3}{2}f_i \\ q_1 = & \frac{1}{2}f_i+\frac{1}{2}f_{i+1} \end{cases} \tag{4}$$

the weight ω_k is constructed as

$$\omega_k=\frac{\alpha_k}{\alpha_0+\alpha_1},\ \alpha_k=\frac{c_k}{(IS_k+\epsilon)^p},\ k=0,1 \tag{5}$$

where, IS_k is the local smoothness indicator that measures the smoothness of numerical solution on the sub-stencil S_k. $c_0 = 1/3$ and $c_1 = 2/3$ are called the optimal weights since they generate the third-order upstream scheme. ϵ is a positive real number introduced to avoid the denominator becoming zero. $\epsilon = 10^{-40}$ is recommended by Henrick et al.[5] and used in this paper. The larger power p can make the weight assigned to the non-smooth sub-stencil approach to zero faster, and also result in more dissipative WENO schemes[8]. Numerical results in [11, 12, 13] showed that $p = 1$ is adequate for a third-order WENO scheme to preserve ENO property and also is used in all tested third-order WENO schemes in this paper.

2.1. The WENO-JS scheme

In [1], Jiang and Shu proposed the classical smoothness indicator as

$$IS_k = \sum_{l=1}^{r-1} \int_{x_{i-1/2}}^{x_{i+1/2}} (\Delta x)^{2l-1} (q_k^{(l)})^2 dx \tag{6}$$

where, $q_k^{(l)}$ is the lth order derivative of $q_k(x)$, and $q_k(x)$ is the interpolation polynomial on sub-stencil S_k. For the third-order WENO scheme, $r = 2$, and
eqrefeq:jiang gives the same formula as those of Liu et al.[2]

$$\begin{cases} IS_0 = & (f_i - f_{i-1})^2 \\ IS_1 = & (f_{i+1} - f_i)^2 \end{cases} \tag{7}$$

In smooth regions, the Taylor series expansions of (7) at x_i give

$$\begin{cases} IS_0 = & (f_i' \Delta x - \frac{1}{2} f_i'' \Delta x^2 + O(\Delta x^3))^2 \\ IS_1 = & (f_i' \Delta x + \frac{1}{2} f_i'' \Delta x^2 + O(\Delta x^3))^2 \end{cases} \tag{8}$$

(8) can be written as

$$IS_k = A(1 + O(\Delta x)) \tag{9}$$

where, A is independent of k. Substituting (9) into (5), we have

$$\omega_k = c_k + O(\Delta x) \tag{10}$$

Similar to the work of Henrick et al.[5], Yamaleev and Carpenter[11] derived the necessary and sufficient conditions that provide third-order convergence of a third-order WENO scheme. A sufficient condition is given by

$$\omega_k = c_k + O(\Delta x^2) \tag{11}$$

Note that (11) imposes a more severe constraint on the weights compared with (10). And numerical experiments[11, 12] also showed that the WENO-JS scheme with the indicators (7) is too dissipative.

2.2. The WENO-M scheme

In [5], Henrick et al. proposed a mapping function to improve the approximation accuracy of ω_k to c_k. The mapping function is defined as

$$g_k(\omega_k) = \frac{\omega_k(c_k + c_k^2 - 3c_k\omega_k + \omega_k^2)}{c_k^2 + \omega_k(1 - 2c_k)} \tag{12}$$

Applying the mapping function, the new weights for the third-order WENO-M scheme are

$$\omega_k^M = \frac{\alpha_k}{\alpha_0 + \alpha_1}, \ \alpha_k = g_k(\omega_k) \tag{13}$$

Using the similar analysis in [5], it is easy to find that

$$\omega_k^M = c_k + O(\Delta x^3) \tag{14}$$

(14) indicates theoretically that the weights (13) go beyond the sufficient condition (11) for a third-order WENO scheme. However, the numerical results (See Section 4.1) showed that the WENO-M scheme cannot reach the third-order accuracy. And hence the issue of improving the third-order WENO scheme is still open.

2.3. The WENO-Z-type schemes

As pointed out by Borges et al.[7], the mapping function used to construct the WENO-M scheme is computationally expensive. Hence, similar as the fifth-order WENO-Z scheme[7], one can easily construct a third-order WENO-Z-type scheme by introducing a global smoothness indicator τ, and the weights are calculated as

$$\omega_k^Z = \frac{\alpha_k}{\alpha_0 + \alpha_1},\ \alpha_k = c_k \left(1 + \frac{\tau}{IS_k + \epsilon}\right) \tag{15}$$

For example, by directly generalizing the method of Borges et al., one can obtain a global smoothness indicator as

$$\tau_3 = |IS_1 - IS_0| \tag{16}$$

Yamaleev and Carpenter[11] proposed a different indicator for the ESWENO scheme as

$$\tau_E = (f_{i-1} - 2f_i + f_{i+1})^2 \tag{17}$$

and Wu and Zhao[12] constructed a indicator for the WENO-N3 scheme as

$$\tau_N = \left| \frac{IS_0 + IS_1}{2} - IS_3 \right| \tag{18}$$

where, $IS_3 = \frac{13}{12}(f_{i-1} - 2f_i + f_{i+1})^2 + \frac{1}{4}(f_{i-1} - f_{i+1})^2$ is the local smoothness indicator at the second sub-stencil $S_1 = (x_{i-1}, x_i, x_{i+1})$ in the fifth-order WENO scheme[1]. In fact, the two indicators (17) and (18) have the same expression as $\tau = \gamma(f_{i-1} - 2f_i + f_{i+1})^2$, in which, $\gamma = 1$ and $\gamma = 5/6$ are taken in (17) and (18), respectively. Hence, in this paper, we only discuss the WENO-N3 scheme with τ_N.

In smooth regions, by means of the Taylor series expansion and simple derivation, one can get

$$\omega_k^{\tau_3} = c_k + O(\Delta x) \tag{19}$$

and

$$\omega_k^{\tau_N} = c_k + O(\Delta x^2), f_i' \neq 0 \tag{20}$$

It should be pointed out that, if $f_i' = 0$, the global smoothness indicator τ_N/τ_E and the local ones (7) have the same order of magnitude. The numerical results in [12] showed that the improved third-order WENO schemes above cannot reach the expected goal.

In [13], Wu et al. proposed a modified indicator $\tau_{NP} = (\tau_N)^p$ $(p = 3/2)$ to construct the WENO-NP3 scheme to improve the accuracy of the WENO-N3 scheme in smooth regions. However, such a modification of τ_N destroys the requirement that the global smoothness indicator and the local ones should have the same dimension. The numerical testing also showed the WENO-NP3 scheme cannot preserve the ENO property. Hence, the third-order WENO-NP3 scheme constructed in [13] is unavailable in applications.

3. THE NEW LOCAL SMOOTHNESS INDICATORS

In this section, we present a new way to calculate the indicators, which are used to replace (7) to improve the third-order WENO scheme.

First, the first-order derivatives of flux f at node $i+1,\ i$ and $i-1$ are approximated by

$$\begin{cases} F'_{i+1} = & \dfrac{3f_{i+1} + f_{i-1} - 4f_i}{2\Delta x} \\ F'_i \quad = & \dfrac{f_{i+1} - f_{i-1}}{2\Delta x} \\ F'_{i-1} = & \dfrac{4f_i - 3f_{i-1} - f_{i+1}}{2\Delta x} \end{cases} \tag{21}$$

Then, the new indicators are constructed as follows

$$\begin{cases} IS_0 = & (|F'_i\Delta x| - |F'_{i-1}\Delta x|)^2 = \dfrac{1}{4}(|f_{i+1} - f_{i-1}| - |4f_i - 3f_{i-1} - f_{i+1}|)^2 \\ IS_1 = & (|F'_i\Delta x| - |F'_{i+1}\Delta x|)^2 = \dfrac{1}{4}(|f_{i+1} - f_{i-1}| - |3f_{i+1} + f_{i-1} - 4f_i|)^2 \end{cases} \tag{22}$$

Next, we discuss the important properties of the new indicators.

Firstly, in monotonic smooth regions, the derivatives $F'_{i-1},\ F'_i$ and F'_{i+1} in (21) have the same sign, thus (22) becomes

$$\begin{cases} IS_0 = & \dfrac{1}{4}\left[f_{i+1} - f_{i-1} - (4f_i - 3f_{i-1} - f_{i+1})\right]^2 = (f_{i+1} - 2f_i + f_{i-1})^2 \\ IS_1 = & \dfrac{1}{4}\left[f_{i+1} - f_{i-1} - (3f_{i+1} + f_{i-1} - 4f_i)\right]^2 = (f_{i+1} - 2f_i + f_{i-1})^2 \end{cases} \tag{23}$$

Hence we have

$$IS_0 = IS_1 \tag{24}$$

Substituting (24) into the weight function (5) of the third-order WENO scheme, there is

$$\omega_0 = c_0,\ \omega_1 = c_1 \tag{25}$$

That means, in monotonic smooth regions, the new weights are exactly equal to the optimal weights, i.e. the fully third-order upstream scheme is recovered. Hence the new indicators (22) do not bring any additional dissipation for the WENO scheme. This property makes the new WENO scheme superior to the others in reducing numerical dissipation.

Secondly, if there is a discontinuity inside a sub-stencil, for example, sub-stencil $S_0 = (i-1,\ i)$, and the other one $S_1 = (i,\ i+1)$ is smooth. Let

$$\begin{cases} \beta_0 = & (f_i - f_{i-1}) \\ \beta_1 = & (f_{i+1} - f_i) \end{cases} \tag{26}$$

Since $|\beta_0|$ is much larger than $|\beta_1|$, i.e. $|\beta_0| \gg |\beta_1|$, the new indicators of (22) can be approximated by

$$\begin{cases} IS_0 = & \frac{1}{4}(|\beta_0 + \beta_1| - |3\beta_0 - \beta_1|)^2 = (\beta_0 + \beta_1)^2 = O(\beta_0^2) \\ IS_1 = & \frac{1}{4}(|\beta_0 + \beta_1| - |3\beta_1 - \beta_0|)^2 = (2\beta_1)^2 = O(\beta_1^2) \end{cases} \tag{27}$$

(27) shows that the new indicators approximate the ones of Jiang and Shu (7). Hence, the ENO property can be maintained for problems with discontinuities.

Finally, at a critical point, $f_i' = 0$, the Taylor series expansions of (22) give

$$\begin{cases} IS_0 = & (|\frac{f_i'''\Delta x^3}{6} + O(\Delta x^5)| + |f_i''\Delta x^2 - \frac{f_i'''\Delta x^3}{6} + O(\Delta x^4)|)^2 \\ IS_1 = & (|\frac{f_i'''\Delta x^3}{6} + O(\Delta x^5)| + |f_i''\Delta x^2 + \frac{f_i'''\Delta x^3}{6} + O(\Delta x^4)|)^2 \end{cases} \tag{28}$$

Similarly, (28) can be expressed as

$$IS_k = B(1 + O(\Delta x)) \tag{29}$$

where B is independent of k. Although the weights with the new indicators (22) do not meet the sufficient condition (11) near the critical points, owing to the advantage in monotonic smooth regions, they can still greatly decrease the numerical dissipation of the third-order WENO scheme, even near critical points.

4. NUMERICAL EXAMPLES

In this section, several linear advection problems, one-dimensional (1-D) and two-dimensional (2-D) Euler problems are calculated to test the performance of the new third-order WENO scheme. The time derivative is approximated with the third-order TVD Runge-Kutta method[14].

4.1. Linear advection problems

In the following we test the accuracy of WENO schemes on the linear advection equation

$$\begin{cases} \dfrac{\partial u}{\partial t} + \dfrac{\partial u}{\partial x} = 0, & x_0 \leqslant x \leqslant x_1 \\ u(x, t=0) = u_0(x), & \text{periodic boundary} \end{cases} \tag{30}$$

The exact solution of (30) is given by

$$u(x,t) = u_0(x - t) \tag{31}$$

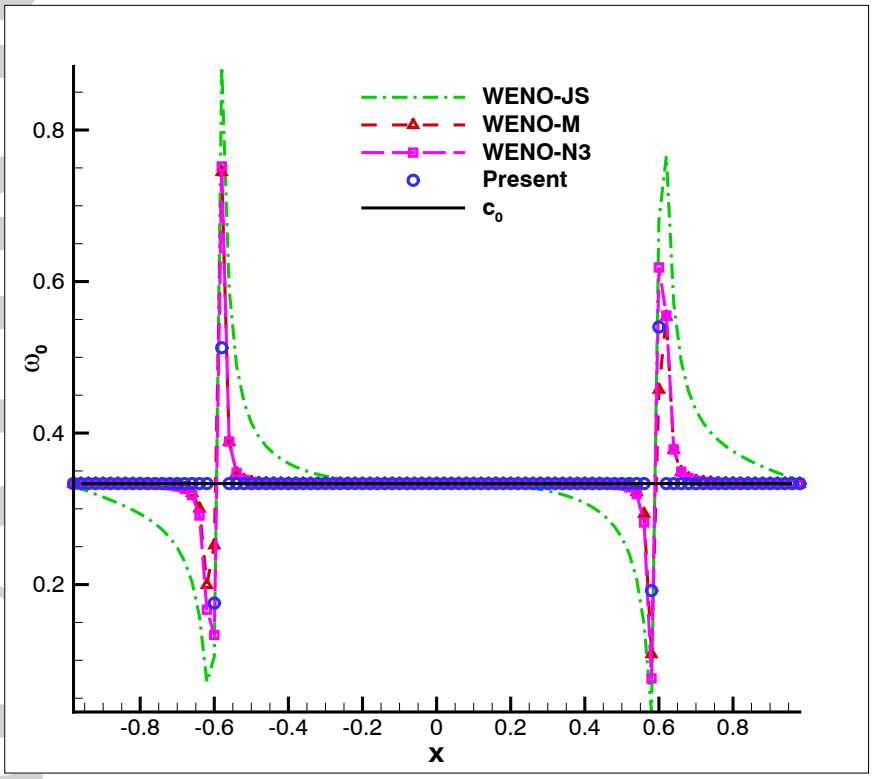

Figure 1. The distribution of ω_0 at initial step $t = 0$ of Case 1

4.1.1. Case 1

$$u_0(x) = \sin\left(\pi x - \frac{\sin \pi x}{\pi}\right), -1 \le x \le 1 \tag{32}$$

This particular initial condition[5] has two critical points at which $f' = 0$ and $f'' \neq 0$. The errors and the convergence order in L_∞ and L_1 norm of the different schemes at $t = 2$ with $\Delta t = 8\Delta x^{5/3}$ are given in Table I. It can be seen that, all improved third-order WENO schemes can not achieve the expected third-order accuracy, but the present one performs best in all tested schemes, the L_1 error of the present scheme is only half of the one of WENO-N3. Fig.1 displays the behavior of the weight ω_0 of different WENO schemes at initial step $t = 0$ with a grid of 100 and shows the weight calculated by present local smoothness indicators is the same as the value of the ideal weight in monotonic smooth regions.

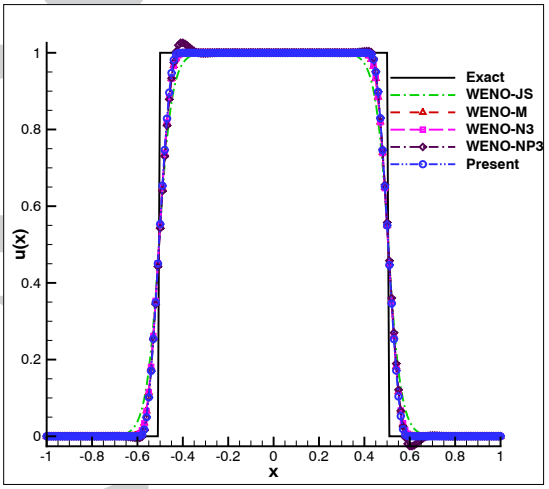

Figure 2. Solution of Case 2

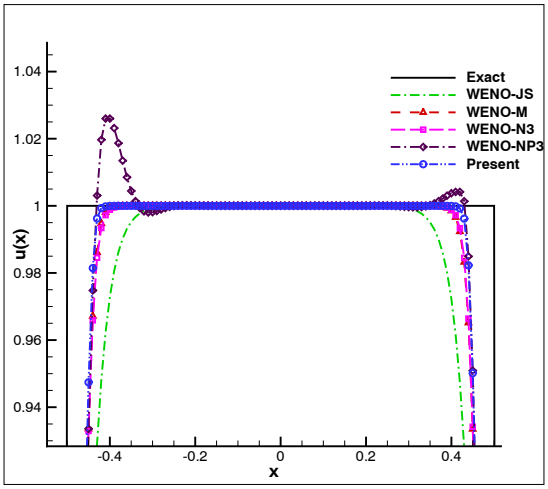

Figure 3. Enlarged plot around discontinuities of Fig.2

Table I. Convergence properties in L_∞ and L_1 norm of linear case

N	WENO-JS		WENO-M	
	L_∞(order)	L_1(order)	L_∞(order)	L_1(order)
100	2.424E-2(—)	9.568E-3(—)	1.575E-2(—)	5.086E-3(—)
200	9.201E-3(1.40)	2.274E-3(2.07)	5.628E-3(1.48)	1.099E-3(2.21)
400	3.418E-3(1.43)	5.170E-4(2.14)	1.954E-3(1.53)	2.242E-4(2.29)
800	1.260E-3(1.44)	1.150E-4(2.17)	6.675E-4(1.55)	4.396E-5(2.35)
1600	4.590E-4(1.46)	2.522E-5(2.18)	2.244E-4(1.57)	8.492E-6(2.37)
N	WENO-N3		Present	
	L_∞(order)	L_1(order)	L_∞(order)	L_1(order)
100	1.666E-2(—)	5.556E-3(—)	1.173E-2(—)	3.284E-3(—)
200	5.977E-3(1.48)	1.204E-3(2.21)	4.003E-3(1.55)	6.760E-4(2.28)
400	2.083E-3(1.52)	2.460E-4(2.29)	1.351E-3(1.57)	1.298E-4(2.38)
800	7.133E-4(1.55)	4.860E-5(2.34)	4.479E-4(1.59)	2.446E-5(2.41)
1600	2.405E-4(1.57)	9.399E-6(2.37)	1.465E-4(1.61)	4.529E-6(2.43)

4.1.2. Case 2

$$u_0(x) = \begin{cases} 1, & \text{if } |x| < 0.5 \\ 0, & \text{otherwise} \end{cases} \tag{33}$$

This case is used to test the shock capturing capability of the WENO schemes. The numerical solution at t=8 with N=200 and time step $\Delta t = \Delta x/2$ are shown in Figs.2 and 3. It can be seen that, as mentioned previously, the WENO-NP3 scheme[13] generates apparent oscillations near discontinuous regions. The present scheme keeps the best behavior.

4.1.3. Case 3

$$u_0(x) = e^{-(x-90)^2/400}\left(\cos\left(\frac{\pi}{8}(x-90)\right) + \cos\left(\frac{\pi}{4}(x-90)\right)\right), 50 \le x \le 130 \tag{34}$$

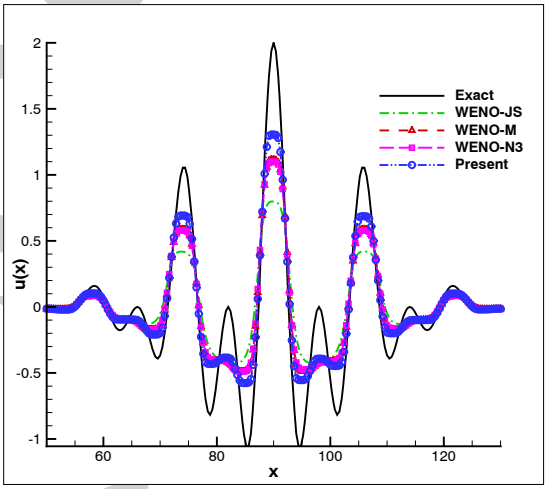

Figure 4. Solution of Case 3

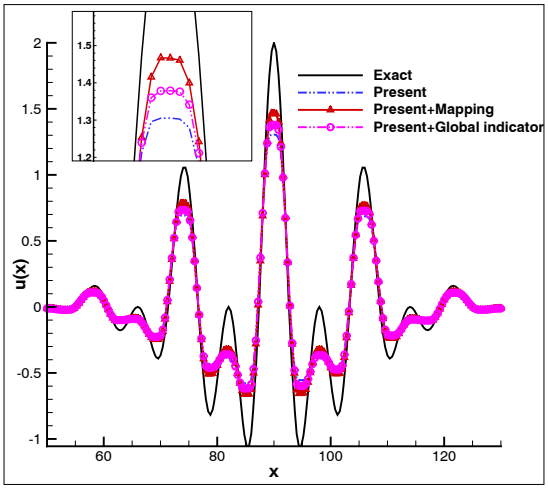

Figure 5. Solution of further improved schemes

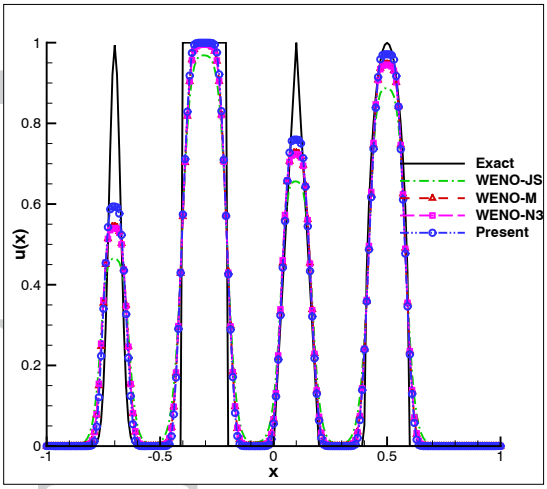

Figure 6. Solution of Case 4

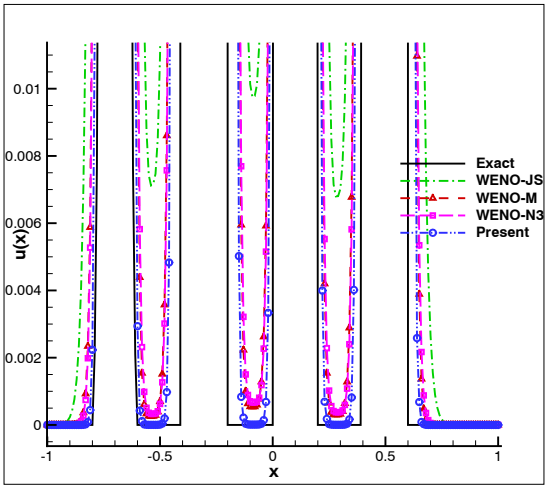

Figure 7. Enlarged plot of Fig.6

This case is used to test the performance of WENO schemes for a smooth solution with several critical points[15]. Fig.4 shows the numerical solutions with grid number $N = 200$ and $\Delta t = \Delta x/2$ at $t = 160$. As mentioned above, although the present scheme cannot achieve optimal convergence order, it still can greatly decrease the dissipation of the WENO scheme, even near critical points.

This example is also calculated by the further improved schemes (WENO-M-type and WENO-Z-type schemes), which are based on the WENO scheme with the new local smoothness indicators (22) and by means of the mapping function (12) of the WENO-M scheme and the global smoothness indicator (16) of the WENO-Z scheme, respectively. The results shown in Fig.5 indicate that the mentioned methods can also be directly used to improve the performance of the new scheme. Since the purpose of this paper is mainly to show the benefits from the new local smoothness indicators, both the further improved schemes are no longer discussed and compared in this paper.

4.1.4. Case 4

$$u(x,0)=\begin{cases}\frac{1}{6}(G(x,\beta,z-\delta)+G(x,\beta,z+\delta)+4G(x,\beta,z)), & -0.8\leqslant x<-0.6\\ 1, & -0.4\leqslant x<-0.2\\ 1-|10(x-0.1)|, & 0\leqslant x<0.2\\ \frac{1}{6}(F(x,\alpha,a-\delta)+F(x,\alpha,a+\delta)+4F(x,\alpha,a)), & 0.4\leqslant x<0.6\\ 0, & \text{otherwise}\end{cases}$$

$$G(x,\beta,z)=e^{-\beta(x-z)^2},F(x,\beta,a)=\sqrt{\max(1-\alpha^2(x-a)^2,0)} \tag{35}$$

This is a classical testing case, which contains a Gaussian, a triangle, a square-wave and a semi-ellipse. It is often used to test the robustness and dissipation of high order schemes. The constants are $z=-0.7,\ \delta=0.005,\ \beta=log(2)/(36\delta^2),\ a=0.5$ and $\alpha=10$. It is solved with $N=200$ and time step $\Delta t=\Delta x/2$. Figs.6 and 7 display the results at $t=2$. Same as shown in the previous case, the present scheme resolves all four waves better than the others.

4.2. Nonlinear Burgers equation (Case 5)

The nonlinear Burgers equation with a periodic boundary condition

$$\begin{cases}\dfrac{\partial u}{\partial t}+\dfrac{\partial(u^2/2)}{\partial x}=0, & -1\leqslant x\leqslant 1,\\ u(x,t=0)=u_0(x), & \text{periodic boundary},\end{cases} \tag{36}$$

is solved as case 5. For the initial data $u_0(x)=\frac{1}{2}+\sin(\pi x)$, the exact solution is smooth up to $t=\frac{1}{\pi}$[2]. We list the errors and orders in Table II. It can be seen that, the present scheme can decrease the errors by about 70% compared with the WENO-JS scheme and by about 40% compared with the other two schemes.

Table II. Convergence properties in L_∞ and L_1 norm of nonlinear case

N	WENO-JS		WENO-M	
	L_∞(order)	L_1(order)	L_∞(order)	L_1(order)
50	8.193E-3(—)	2.152E-3(—)	6.219E-3(—)	1.380E-3(—)
100	3.377E-3(1.28)	4.536E-4(2.25)	2.527E-3(1.30)	2.996E-4(2.20)
200	1.298E-3(1.38)	1.014E-4(2.16)	1.954E-3(1.53)	2.242E-4(2.29)
400	4.890E-4(1.41)	2.330E-5(2.12)	3.266E-4(1.50)	1.286E-5(2.31)
800	1.835E-4(1.41)	5.215E-6(2.16)	1.156E-4(1.50)	2.624E-6(2.30)
N	WENO-N3		Present	
	L_∞(order)	L_1(order)	L_∞(order)	L_1(order)
50	6.297E-3(—)	1.420E-3(—)	4.705E-3(—)	1.101E-3(—)
100	2.589E-3(1.28)	3.072E-4(2.21)	1.995E-3(1.24)	2.278E-4(2.28)
200	9.446E-4(1.45)	6.582E-5(2.22)	7.064E-4(1.50)	4.221E-5(2.38)
400	3.354E-4(1.49)	1.330E-5(2.31)	2.432E-4(1.54)	8.426E-6(2.41)
800	1.189E-4(1.50)	2.720E-6(2.29)	8.408E-5(1.53)	1.614E-6(2.43)

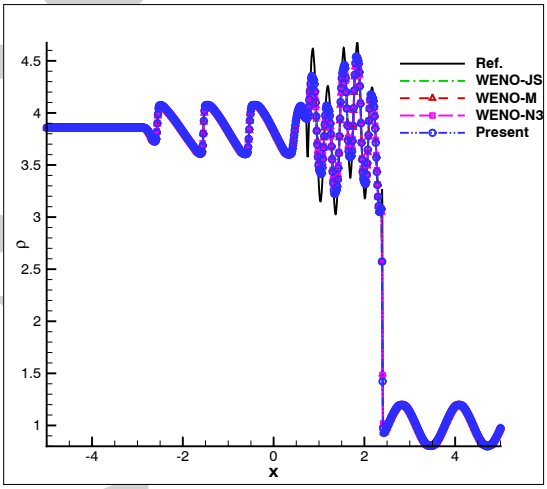

Figure 8. Solution of Case 6

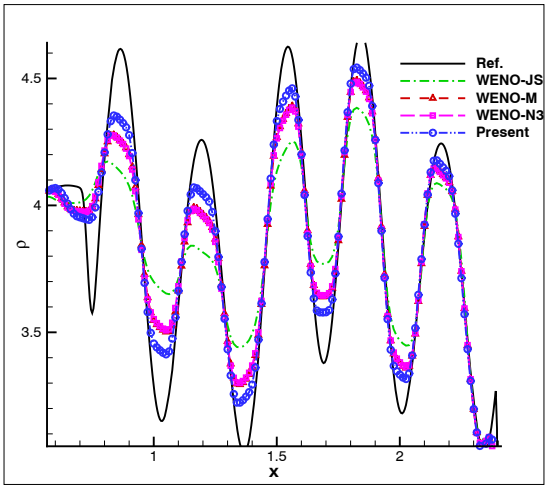

Figure 9. Enlarged plot of Fig.8

4.3. *One-dimensional Euler problems*

The governing equations are as follows

$$\frac{\partial U}{\partial t}+\frac{\partial F}{\partial x}=0 \tag{37}$$

where $U=(\rho,\rho u,E)^T,\ F(U)=\left(\rho u,\rho u^2+p,u(E+p)\right)^T.\ \rho,\ u,\ E,\ p$ are the density, velocity, total energy and pressure, respectively. For ideal gas, $E=p/(\gamma-1)+\rho u^2/2.\ \gamma=1.4$ is the ratio of specific heat. Time step is taken as

$$\Delta t=\frac{\sigma\Delta x}{\max_i\left(|u_i|+c_i\right)} \tag{38}$$

where, σ is CFL number, and 0.5 is used for all four 1-D cases in this subsection. c, the speed of sound, is given by $c=\sqrt{\gamma p/\rho}$. The local LF flux-splitting method is used and the WENO reconstruction is carried out in local characteristic fields[11]. All the reference solutions were obtained by the WENO-JS scheme with 2000 points.

4.3.1. Case 6 The first 1-D case is Shu-Osher problem[14], its initial condition is given as follows

$$(\rho,\ u,\ p)=\begin{cases}(3.857143,\ 2.629369,\ 31/3) & -5\le x<-4\\ (1+0.2\sin(5x),\ 0,\ 1) & -4\le x\le 5\end{cases} \tag{39}$$

Figs.8 and 9 give the density distribution at $t=1.8$ by using $N=800$. As shown in the scalar case 3, for the solution with high frequency, the present scheme shows apparent improvement over the others.

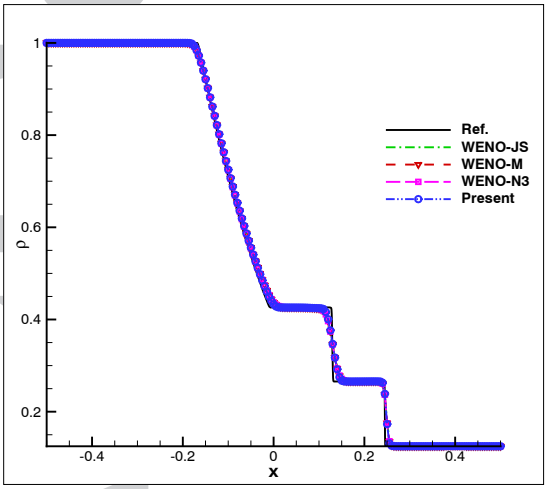

Figure 10. Solution of Case 7

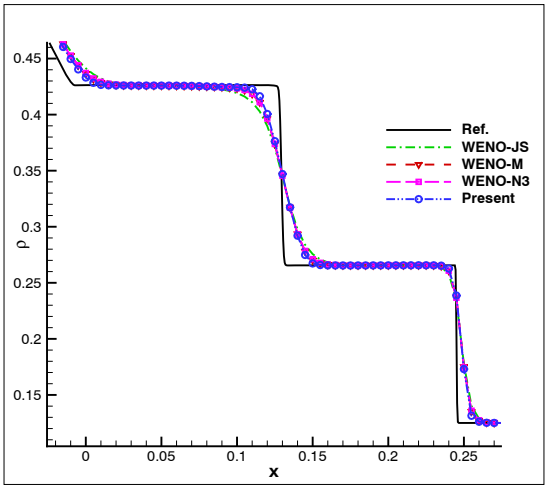

Figure 11. Enlarged plot of Fig.10

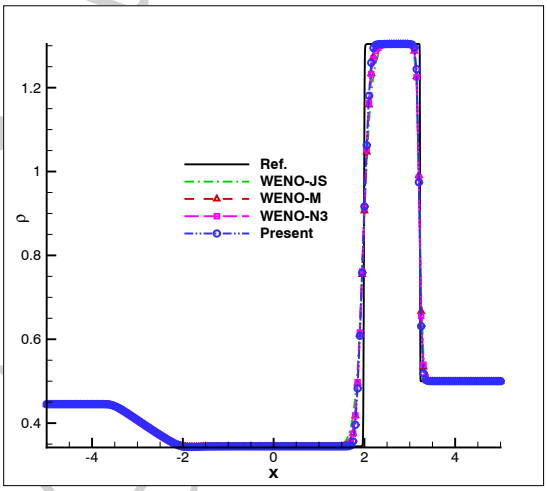

Figure 12. Solution of Case 8

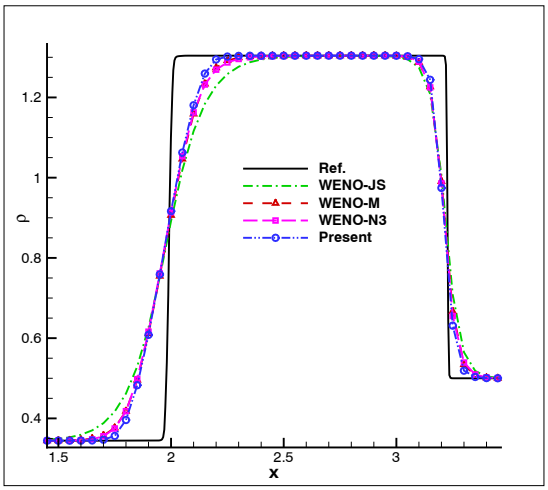

Figure 13. Enlarged plot of Fig.12

4.3.2. Case 7 The second 1-D case is Sod problem, with initial condition

$$(\rho,\ u,\ p) = \begin{cases} (0.125,\ 0,\ 0.1) & 0.5 \le x \le 1 \\ (1,\ 0,\ 1) & 0 \le x < 0.5 \end{cases} \tag{40}$$

It is solved with $N = 200$ at $t = 0.14$. The results in Figs.10 and 11 show that the new scheme can capture shocks and contact discontinuities well.

4.3.3. Case 8 The third 1-D case is Lax problem[7], with initial condition

$$(\rho,\ u,\ p) = \begin{cases} (0.445,\ 0.698,\ 3.528) & -5 \le x < 0 \\ (0.5,\ 0,\ 0.571) & 0 \le x \le 5 \end{cases} \tag{41}$$

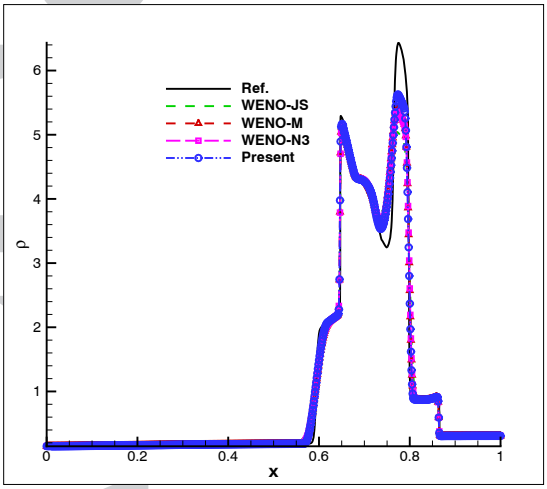

Figure 14. Solution of Case 9

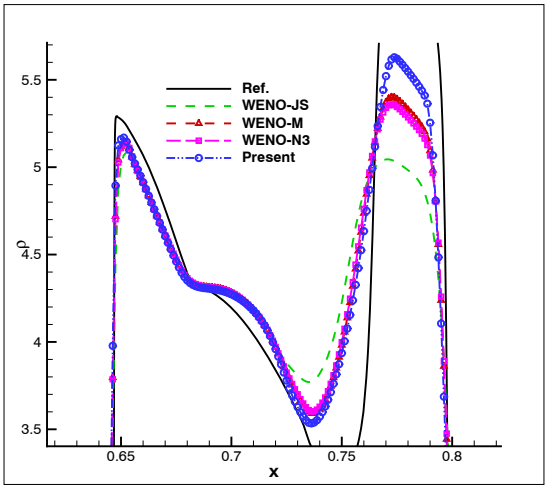

Figure 15. Enlarged plot of Fig.14

It is solved with $N = 200$ at $t = 1.3$. The density distribution is displayed in Figs.12 and 13. The new scheme obtains sharper shock profiles than the others.

4.3.4. Case 9 The last one is the blast-waves interaction problem[7], with initial condition

$$(\rho,\ u,\ p) = \begin{cases} (1,\ 0,\ 1000) & 0 \le x < 0.1 \\ (1,\ 0,\ 0.001) & 0.1 \le x < 0.9 \\ (1,\ 0,\ 100) & 0.9 \le x \le 1 \end{cases} \tag{42}$$

The numerical results at $t = 0.038$ with $N = 800$ are presented in Figs.14 and 15. As previously discussed, the new scheme can obtain more accurate solutions near extrema.

4.4. Two-dimensional Euler problems

In this subsection, we further study the shock capturing ability and numerical dissipation of the new scheme in the 2-D problems. The 2-D Euler equations are solved,

$$\frac{\partial U}{\partial t} + \frac{\partial F}{\partial x} + \frac{\partial G}{\partial y} = 0 \tag{43}$$

where the conserved variables U and the inviscid flux vectors F and G are

$$U = \begin{bmatrix} \rho \\ \rho u \\ \rho v \\ E \end{bmatrix},\ F = \begin{bmatrix} \rho u \\ \rho u^2 + p \\ \rho uv \\ Eu + pu \end{bmatrix},\ G = \begin{bmatrix} \rho v \\ \rho uv \\ \rho v^2 + p \\ Ev + pv \end{bmatrix} \tag{44}$$

The energy is given by

$$E = \frac{p}{\gamma - 1} + \frac{\rho}{2}(u^2 + v^2) \tag{45}$$

The Roe[16] flux-splitting method is used for the inviscid convective fluxes, and the time step is taken as follows

$$\Delta t = \sigma \frac{\Delta t_x \Delta t_y}{\Delta t_x + \Delta t_y}$$
$$\begin{cases} \Delta t_x = & \dfrac{\Delta x}{max_{i,j}\left(|u_{i,j}| + c_{i,j}\right)} \\ \Delta t_y = & \dfrac{\Delta y}{max_{i,j}\left(|v_{i,j}| + c_{i,j}\right)} \end{cases} \tag{46}$$

where, σ is CFL number, and 0.5 is used for all the tests below.

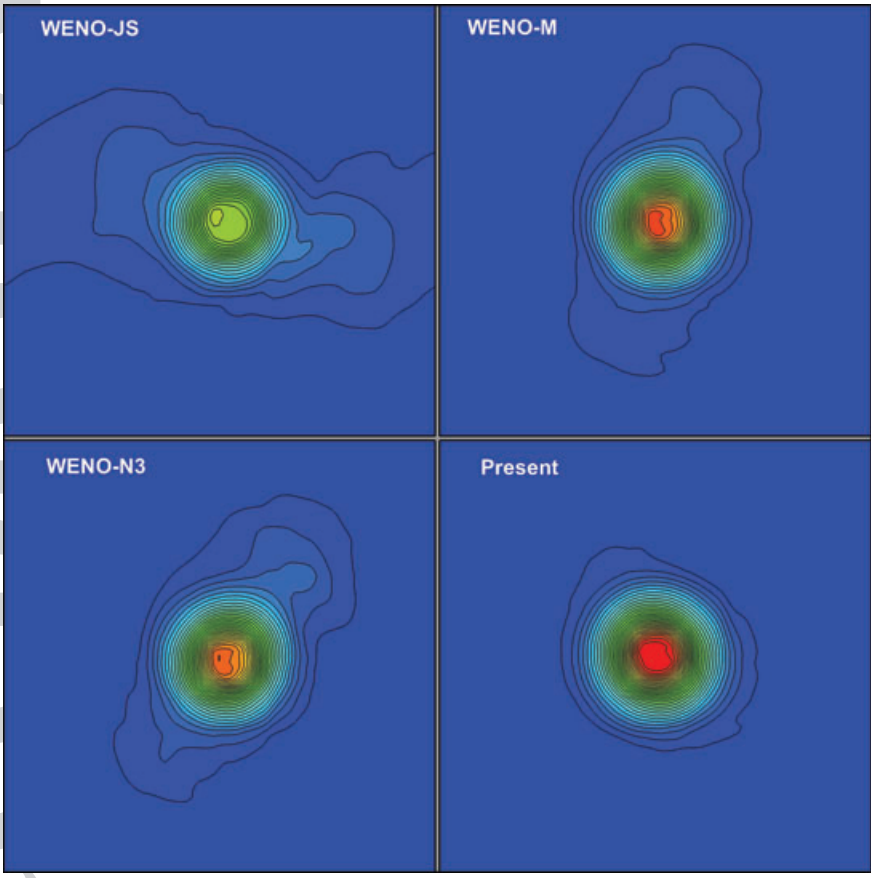

Figure 16. Density contours of Case 10, 30 contours from 0.63 to 0.99

4.4.1. Case 10 This is a 2-D periodic vortex propagation problem[17, 18] used to assess the numerical dissipation of different schemes. The vortex is described as a perturbation to the velocity

$(u,\ v)$, temperature $(T = p/\rho)$ and entropy $(S = p/\rho)$ of the mean flow $(\rho,\ u,\ v,\ p) = (1,\ 1,\ 1,\ 1)$

$$\begin{cases} \hat{u} = -\dfrac{\epsilon e^{(1-r^2)/2}}{2\pi}\bar{y} \\ \hat{v} = \dfrac{\epsilon e^{(1-r^2)/2}}{2\pi}\bar{x} \\ \hat{T} = -\dfrac{(\gamma-1)\epsilon^2 e^{(1-r^2)}}{8\gamma\pi^2} \\ \hat{S} = 0 \end{cases} \tag{47}$$

where, $(\bar{x},\ \bar{y}) = (x-5,\ y-5)$, $r^2 = \bar{x}^2 + \bar{y}^2$, and the vortex strength $\epsilon = 5.0$. The computational domain is $[0,\ 10] \times [0,\ 10]$, and periodic boundary condition is used in both directions. It can be readily verified that the Euler equations with the above initial conditions admit an exact solution that moves with the speed (1,1) in the diagonal direction. The errors based on the density of the WENO-M, WENO-N3 and the present schemes are presented in Table III. The present scheme reduces errors by about 70% compared with WENO-JS and by about 45% compared with the other two schemes.

The results are also carried out until $t = 100$ with a grid of 80×80, to further demonstrate the low dissipation of the new scheme. Fig.16 shows the density contours of the WENO schemes. Figs.17 and 18 show the pressure distribution along x-axis at $y = 5$ and the evolution of kinetic energy E_k, respectively. The kinetic energy is calculated by $E_k = \sum_{i,j=(1,1)}^{N,M} \rho_{i,j}(u_{i,j}^2 + v_{i,j}^2)/(2N \times M)$, where N and M are the total cells in x and y direction of the grid, respectively. From these figures, it can be seen that, the WENO-JS scheme is too dissipative, while the present scheme has lowest dissipation.

Table III. Errors for periodic vortex propagation problem at $t = 10$

Grid	WENO-JS		WENO-M	
	L_∞(order)	L_1(order)	L_∞(order)	L_1(order)
20×20	4.153E-1(—)	2.083E-2(—)	3.887E-1(—)	1.881E-2(—)
40×40	1.834E-1(1.18)	9.525E-3(1.29)	1.500E-1(1.37)	6.511E-3(1.53)
80×80	6.652E-2(1.46)	2.937E-3(1.70)	6.850E-2(1.13)	1.825E-3(1.83)
160×160	4.165E-2(0.66)	1.084E-3(1.44)	3.393E-2(1.01)	4.998E-4(1.87)
320×320	1.964E-2(1.08)	2.965E-4(1.87)	1.004E-2(1.76)	1.062E-4(2.23)
Grid	WENO-N3		Present	
	L_∞(order)	L_1(order)	L_∞(order)	L_1(order)
20×20	3.944E-1(—)	1.927E-2(—)	3.670E-1(—)	1.696E-2(—)
40×40	1.527E-1(1.37)	6.746E-3(1.51)	1.400E-1(1.39)	5.291E-3(1.68)
80×80	7.060E-2(1.11)	1.972E-3(1.77)	5.756E-2(1.28)	1.454E-3(1.86)
160×160	3.453E-2(1.03)	5.732E-4(1.78)	2.422E-2(1.25)	3.321E-4(2.13)
320×320	1.020E-2(1.76)	1.130E-4(2.34)	5.336E-3(2.18)	6.359E-5(2.38)

4.4.2. Case 11 The 2-D shock/vortex interaction problem describes an interaction between a stationary shock and a vortex[1]. The computational domain is taken to be $[0,\ 2] \times [0,\ 1]$. A stationary Mach 1.1 shock is positioned at $x = 0.5$ and normal to the x-axis. Its left state is

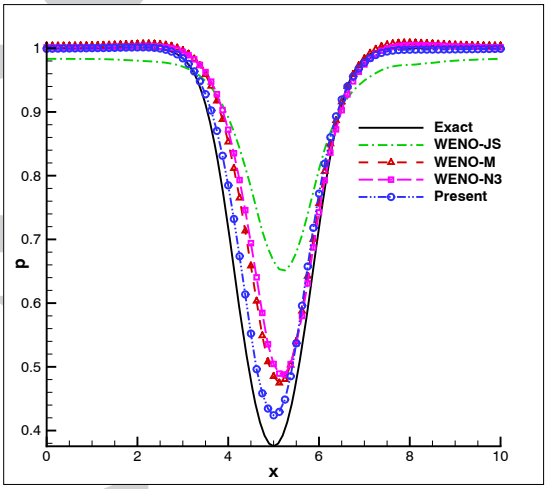

Figure 17. Pressure distributed along $y = 5$ of Case 10

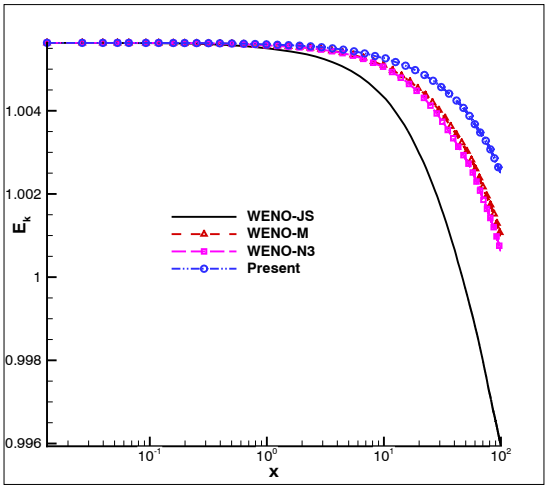

Figure 18. Evolution of E_k of Case 10

$(\rho,\ u,\ v,\ p) = (1,\ 1.1\sqrt{\gamma},\ 0,\ 1)$. A small vortex is superimposed to the flow on the left of the shock and centered at $(x_c,\ y_c) = (0.25,\ 0.5)$. The vortex is described as a perturbation to the velocity $(u,\ v)$, temperature $(T = p/\rho)$ and entropy $S = ln(p/\rho^{\gamma})$ of the mean flow

$$\begin{cases} \hat{u} = \epsilon\tau e^{a(1-\tau^2)}\sin\theta \\ \hat{v} = -\epsilon\tau e^{a(1-\tau^2)}\cos\theta \\ \hat{T} = -\dfrac{(\gamma-1)\epsilon^2 e^{2a(1-\tau^2)}}{4a\gamma} \\ \hat{S} = 0 \end{cases} \tag{48}$$

where, $\tau = r/r_c,\ r = \sqrt{(x-x_c)^2+(y-y_c)^2},\ \epsilon = 0.3,\ r_c = 0.05$ and $a = 0.204$ are the same as in Refs.[1, 19]. The upper and lower boundaries are set to be reflective. The results at $t = 0.6$ with a grid of 100×50 are solved. Fig. 19 is the pressure distribution along the center line of $y = 0.5$. The result obtained by WENO-JS with a refined mesh of 2000×1000 is given as the reference solution. It can be seen that the present scheme obtained most accurate solution near the center of the vortex.

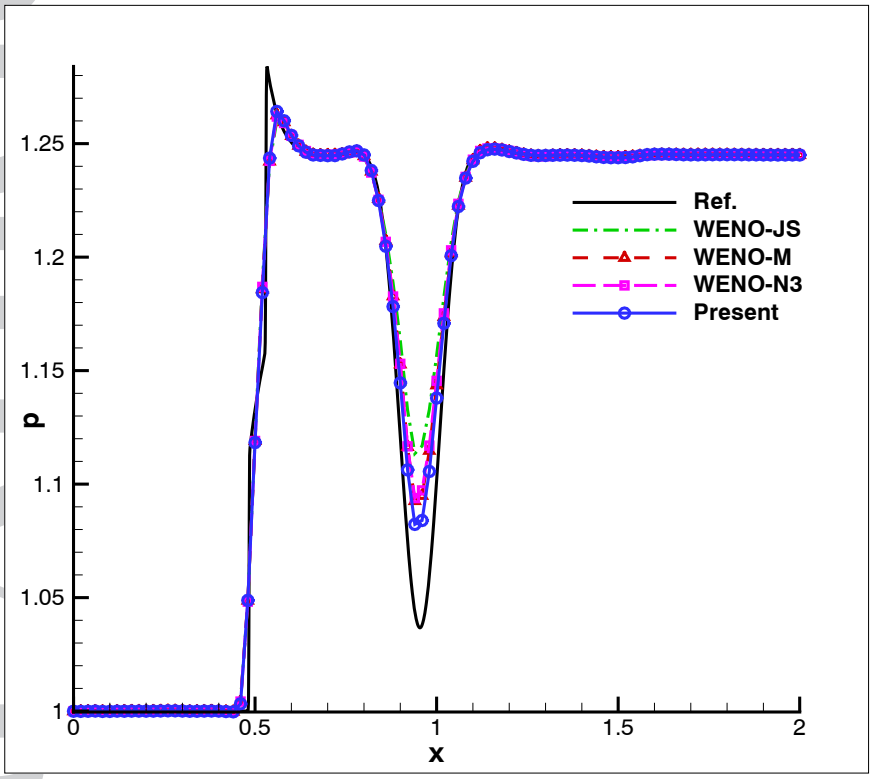

Figure 19. Pressure distributed along $y = 0.5$ of Case 11

4.4.3. Case 12 This is a 2-D Riemann problem[20] used to test the shock capturing capability of the present scheme for calculating shock/shock interaction problems. It is solved on a unit square with initial condition

$$(\rho,\ u,\ v,\ p) = \begin{cases} (1.0,\ -0.75,\ -0.5,\ 1.0), & 0.5 \le x \le 1,\ 0.5 \le y \le 1 \\ (2.0,\ -0.75,\ 0.5,\ 1.0), & 0 \le x < 0.5,\ 0.5 \le y \le 1 \\ (1.0,\ 0.75,\ 0.5,\ 1.0), & 0 \le x < 0.5,\ 0 \le y < 0.5 \\ (3.0,\ 0.75,\ -0.5,\ 1.0), & 0.5 \le x \le 1,\ 0 \le y < 0.5 \end{cases} \tag{49}$$

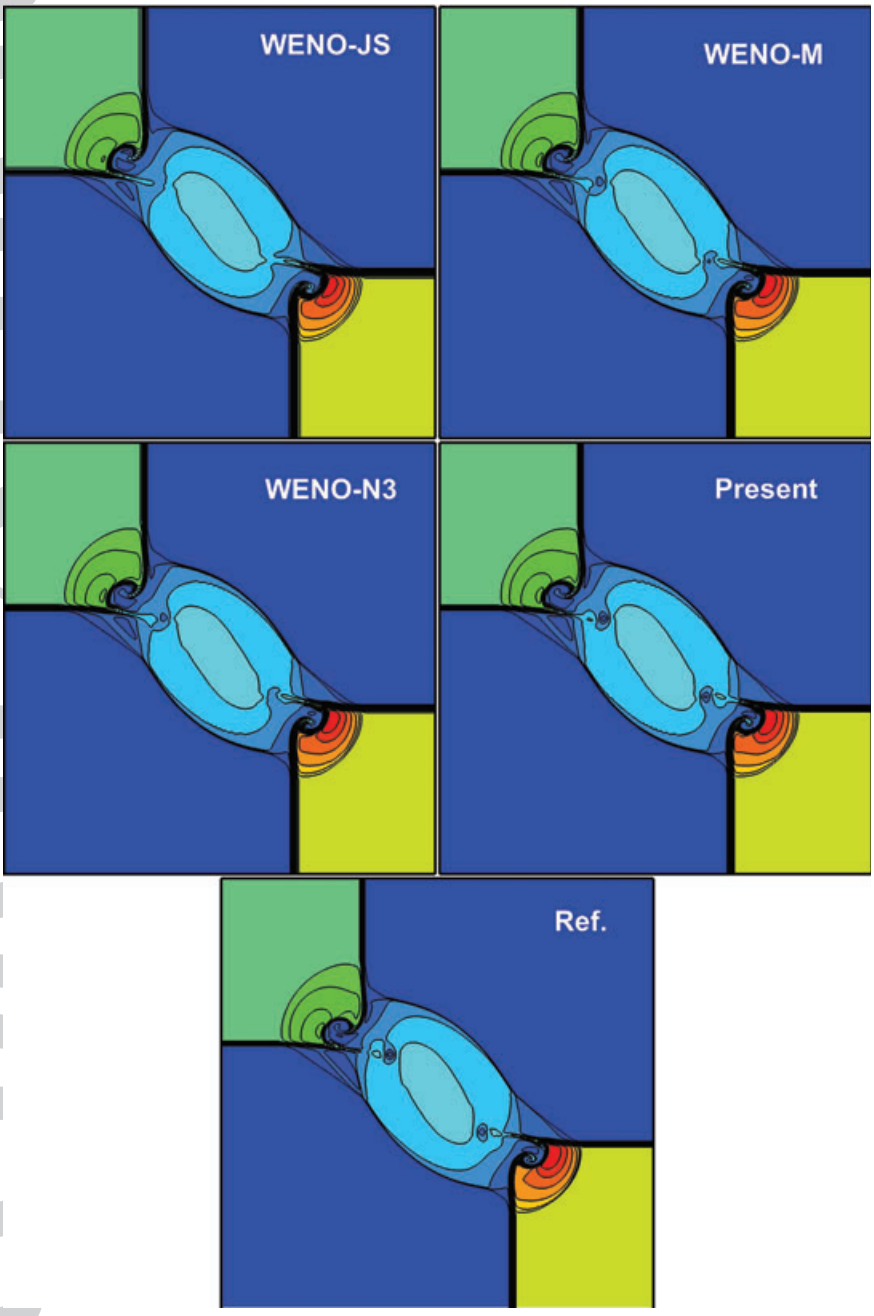

Figure 20. Results of Case 12, 20 contours from 1.1 to 3.8

The solution at $t = 0.23$ is solved with a grid of 400×400. The reference is calculated by WENO-JS with a grid of 800×800. Fig.20 shows the density contours of the reference solution and the results of different WENO schemes. As the figure shows, the present scheme obtained rich structures similar as those obtained by WENO-JS with refined meshes.

5. CONCLUSION REMARKS

In this paper, a new method is proposed to calculate the local smoothness indicators for the third-order WENO scheme by using all the three points on the global stencil. Since the two new indicators are exactly the same in monotonic smooth regions, the weights of the new WENO scheme are equal to the optimal weights, and this property makes the new scheme recover the fully third-order upstream scheme. The numerical results demonstrate that the WENO scheme with the new indicators has less dissipation and better resolution than the ones of Jiang and Shu for both smooth and discontinuous solutions.

Although this paper only focuses on the advantages brought by the new indicators, those methods, such as the mapping function used in the WENO-M scheme and the global smoothness indicator used in the WENO-Z scheme, can also directly be used to further improve the performance of the new third-order WENO scheme.

ACKNOWLEDGEMENT

This research work was supported by NSAF No. U1530145, 2016YFA0401200, SCP No. TZ201*002 and NSFC No. 11272325.

REFERENCES

1. Guang-Shan Jiang and Chi-Wang Shu. Efficient Implementation of Weighted ENO Schemes. *Journal of Computational Physics*, 126:202 – 228, 1996.
2. Xu-Dong Liu, Stanley Osher, and Tony Chan. Weighted Essentially Non-Oscillatory Schemes. *Journal of Computational Physics*, 115:200 – 212, 1994.
3. A. Harten. High resolution schemes for hyperbolic conservation laws. *Journal of Computational Physics*, 49:357 – 393, 1983.
4. Dinshaw S. Balsara and Chi-Wang Shu. Monotonicity Preserving Weighted Essentially Non-oscillatory Schemes with Increasingly High Order of Accuracy. *Journal of Computational Physics*, 160:405 – 452, 2000.
5. Andrew K. Henrick, Tariq D. Aslam, and Joseph M. Powers. Mapped weighted essentially non-oscillatory schemes: Achieving optimal order near critical points. *Journal of Computational Physics*, 207:542 – 567, 2005.
6. G.A. Gerolymos, D. Senechal, and I. Vallet. Very-high-order WENO schemes. *Journal of Computational Physics*, 228:8481 – 8524, 2009.
7. Rafael Borges, Monique Carmona, Bruno Costa, and Wai Sun Don. An improved weighted essentially non-oscillatory scheme for hyperbolic conservation laws. *Journal of Computational Physics*, 227:3191 – 3211, 2008.
8. Marcos Castro, Bruno Costa, and Wai Sun Don. High order weighted essentially non-oscillatory WENO-Z schemes for hyperbolic conservation laws. *Journal of Computational Physics*, 230:1766 – 1792, 2011.
9. Youngsoo Ha, Chang Ho Kim, Yeon Ju Lee, and Jungho Yoon. An improved weighted essentially non-oscillatory scheme with a new smoothness indicator. *Journal of Computational Physics*, 232:68 – 86, 2013.
10. Ping Fan, Yiqing Shen, Baolin Tian, and Chao Yang. A new smoothness indicator for improving the weighted essentially non-oscillatory scheme. *Journal of Computational Physics*, 269:329 – 354, 2014.
11. Nail K Yamaleev and Mark H Carpenter. Third-order energy stable WENO scheme. *Journal of Computational Physics*, 228:3025–3047, 2009.
12. Xiaoshuai Wu and Yuxin Zhao. A high-resolution hybrid scheme for hyperbolic conservation laws. *International Journal for Numerical Methods in Fluids*, 78:162–187, 2015.
13. Xiaoshuai Wu, Jianhan Lian, and Yuxin Zhao. A new smoothness indicator for third-order WENO scheme. *International Journal for Numerical Methods in Fluids*, 81:451–459, 2016.

14. Chi-Wang Shu and Stanley Osher. Efficient implementation of essentially non-oscillatory shock-capturing schemes. *Journal of Computational Physics*, 77:439 – 471, 1988.
15. A. Najiafi-Yazdi and L. Mongeau. A low-dispersion and low-dissipation implicit Runge-Kutta scheme. *Journal of Computational Physics*, 233:315 – 323, 2013.
16. Philip L Roe. Approximate Riemann solvers, parameter vectors, and difference schemes. *Journal of computational physics*, 43:357–372, 1981.
17. Yu-Zhi Sun and Z.J. Wang. Evaluation of discontinuous Galerkin and spectral volume methods for scalar and system conservation laws on unstructured grids. *International Journal for Numerical Methods in Fluids*, 45:819 – 838, 2004.
18. F. Davoudzadeh, H. McDonald, and B.E. Thopson. Accuracy evaluation of unsteady CFD numerical schemes by vortex preservation. *Computational & Fluids*, 24:883 – 895, 1995.
19. Yi-Qing Shen and Guo-Wei Yang. Hybrid finite compact-WENO schemes for shock calculation. *International Journal for Numerical Methods in Fluids*, 53:531 – 560, 2007.
20. Eitan Tadmor Alexander Kurganov. Solution of two-dimensional Riemann problems for gas dynamics without Riemann problem solvers. *Numerical Methods for Partial Differential Equations*, 18:584–608, 2002.